ISSN 1063-7761, Journal of Experimental and Theoretical Physics, 2020, Vol. 131, No. 1, pp. 177–188. © Pleiades Publishing, Inc., 2020.
Russian Text © The Author(s), 2020, published in Zhurnal Eksperimental'noi i Teoreticheskoi Fiziki, 2020, Vol. 158, No. 1, pp. 184–197.

Weak Antiferromagnet Iron Borate $FeBO_3$. Classical Object for Magnetism and the State of the Art

S. G. Ovchinnikov[a,*], V. V. Rudenko[a,], N. V. Kazak[a], I. S. Edelman[a], and V. A. Gavrichkov[a]**

[a] *Kirensky Institute of Physics, Siberian Branch, Russian Academy of Sciences, Krasnoyarsk, 660036 Russia*

**e-mail: sgo@iph.krasn.ru*

***e-mail: rvv@iph.krasn.ru*

Received January 31, 2020; revised March 4, 2020; accepted March 5, 2020

Abstract—The simple lattice and magnetic structure, the high Néel temperature, the narrow antiferromagnetic resonance line of $FeBO_3$, and the narrow electron paramagnetic resonance line of its isostructural diamagnetic analogs MBO_3:Fe^{3+} (M = Ga, In, Sc, Lu) make iron borate unique for investigations and applications. Iron borate is a model crystal for numerous experimental and theoretical studies, including spin crossovers and metallization at megabar pressures and many-electron effects in optics and X-ray spectroscopy. The recent works dealing with the investigation of the properties of $FeBO_3$ are reviewed.

DOI: 10.1134/S106377612007016X

1. INTRODUCTION

$FeBO_3$ crystals have two antiferromagnetic sublattices with a low canting angle between them and represent a typical example of weak ferromagnets, the discovery and investigation of which are related to A.S. Borovik-Romanov and its works in the late 1950s. A weak ferromagnet moment in transition metal carbonates with a rhombohedral calcite structure MCO_3 (M = Mn, Ni, Co), which are isostructural to the $FeBO_3$ iron borate [1], was revealed in those works. Before those works, weak ferromagnetism was only observed in natural, i.e., rather dirty, hematite crystals and was attributed to impurities. The use of high-sensitivity experimental equipment and high-purity synthetic crystals allowed Borovik-Romanov to comprehensively study this unusual phenomenon, to show that the detected magnetism is the intrinsic property of an antiferromagnetic structure, which is not associated with the contamination of samples, and to advance an idea (which was unusual for that time) that the spins in these antiferromagnets are not exactly collinear. Borovik-Romanov et al. [1–4] experimentally studied the main static and resonance properties of rhombohedral MCO_3 crystals and hematite and laid the basis of a phenomenological description of weak ferromagnetism.

Bernal et al. [5] was the first to synthesize the $FeBO_3$ compound in 1963 when studying the reactions between metal and boron oxides. He described the technology of solution–melt solidification of thin yellow–green single-crystal plates (in particular, $Fe_{0.9}Ga_{0.1}BO_3$) using a borate–lead solvent. In the Soviet Union, Seleznev and Rudenko [6] were the first to synthesize iron borate crystals in the Kirensky Institute of Physics in 1972, and the crystals were in great demand in the leading scientific institutes of the country [7–9]. Later, Seleznev and Rudenko transferred their technology to V.I. Vernadsky Crimean Federal University (Simferopol). Large iron borate crystals were synthesized using gas transport [10] and from a solution–melt [11] (see also [12, 13]). Thin $FeBO_3$ films on single-crystal $GaBO_3$ substrates were recently synthesized at V.I. Vernadsky Crimean Federal University [14].

$FeBO_3$ crystals occupy a specific place in the family of borates. This compound has a simple trigonal lattice (calcite structure) with space group $R\bar{3}c$, a high Néel temperature (348 K), narrow antiferromagnetic resonance line, and a series of isostructural diamagnetic analogs. The isostructural crystals of nonmagnetic MBO_3 (M = Ga, In, Sc, Lu) analogs with an Fe^{3+} impurity were used to study electron paramagnetic resonance to quantitatively describe the anisotropy of magnetically ordered $FeBO_3$ crystals [15]. Although the iron borate has been much studied, this crystal attracts attention of researchers as a convenient object for investigating new magnetic properties, which manifest themselves, in particular, in experiments of ultrafast magnetic dynamics [16] and at ultrahigh pressures [17]. In addition, the investigations of the magnetic properties of $FeBO_3$ crystals as mode objects make it possible to extend our knowledge of the nature of magnetic anisotropy, in particular, the Dzyaloshinskii–Moriya interaction (DMI) [18]. The

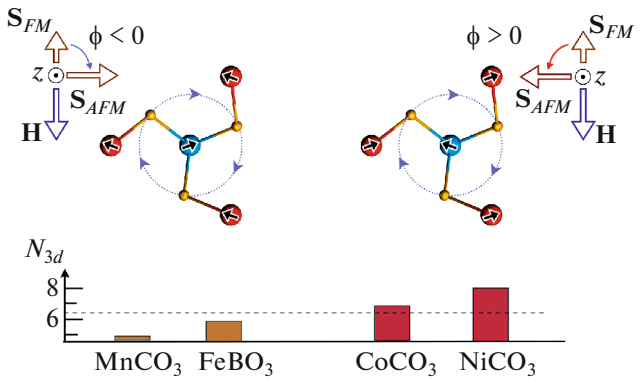

Fig. 1. (Color online) Local atomic and magnetic orders in MCO_3 (M = Mn, Ni, Co) and $FeBO_3$ (borrowed from [27]).

experiments on these crystals [19–22] were performed to stimulate and test the many-electron Mott–Hubbard theory of the electronic structure of insulators, which is developed and known as the generalized tight-binding method [23–26].

In this work, we briefly review the results of studying $FeBO_3$ crystals which were published in recent literature, and obtained in our team. This article has the following structure. In Section 2, we discuss the results of determining the magnitude and sign of DMI; in Section 3, we discuss new data on the nature of magnetic anisotropy. Section 4 is devoted to a review of the available data on magnetoelastic oscillations, Section 5 presents theoretical and experimental results on electronic structure, and Section 6 considers the change in the magnetic and electronic properties during spin crossover in the high-pressure (ultrahigh-pressure) phase.

2. DETERMINATION OF THE MAGNITUDE AND SIGN OF THE DZYALOSHINSKII–MORIYA INTERACTION

Iron borate has a simple calcite lattice. The rhombohedral unit cell has two trivalent iron ions, which are coupled by antiferromagnetically with small DMI-induced canting of sublattices magnetic moments away from antiparallel configuration. In a two-sublattice antiferromagnet with an even (with respect to the principal axis) antiferromagnetic structure, DMI $\mathbf{D}[\mathbf{s}_1 \times \mathbf{s}_2]$, where $\mathbf{s}_1$ and $\mathbf{s}_2$ are the spins of neighboring ions belonging to different magnetic sublattices, is characterized by vector $\mathbf{D}$. It should be noted that only the modulus of vector $\mathbf{D}$ is usually determined in experiments. The authors of [18] recently determined the sign of the Dzyaloshinskii–Moriya vector in $FeBO_3$ using an experimental approach based on the interference of magnetic and resonance X-ray scattering, which was supplemented with the rotation of antiferromagnetic moments by an applied magnetic field. These results were comprehensively considered in our review [15]; therefore, in this work we focus on some works published later. Both the sign and magnitude of DMI in weak ferromagnets, in particular, $FeBO_3$, were qualitatively explained in [27]. DMI manifests itself in magnetic materials at least when inversion is locally broken [28, 29]. As a result, exchange energy, which is described by the vector product of spins $\mathbf{s}_1 \times \mathbf{s}_2$, appears; therefore, the exchange becomes antisymmetric and brings about noncollinear ordering.

The ions of the two magnetic sublattices are shown by blue (site *1*) and red (site *2*) spheres in Fig. 1 with alternating black arrows indicating the spin directions. The oxygen atoms between two transition metal (TM) ion layers are shown as yellow spheres. The dotted arcs indicate the rotation of the oxygen layer. The left- and right-hand sides show possible magnetic configurations, which are stabilized depending on the sign of DMI. $\mathbf{S}_{AFM}$ indicates the antiferromagnetism vector direction. The structural rotation of the oxygen layers with respect to the TM layers shifts oxygen atoms from the midpoint between TM atoms and violates the inversion symmetry in oxygen sites, which leads to DMI between the TM layers. The sign of this rotation alternates from layer to layer, so that the crystal as a whole remains centrosymmetrical. The magnetic moments lie in the basal plane and are parallel inside the TM layer and antiparallel between neighboring layers. However, due to DMI, the antiferromagnetic arrangement is incompletely collinear: small in-plane canting exists in the same direction for all spins, which causes macroscopic magnetization. The canting of sublattice spins is the manifestation of DMI in both magnitude and sign. Table 1 gives the experimental and calculated DMI-induced deviations in degrees [27].

The authors of [27] also performed experiments on diffraction of polarized X rays to determine the sign of canting of the magnetic moments of the sublattices in $FeBO_3$ and compared their results with the results obtained on three other weak ferromagnets ($MnCO_3$, $CoCO_3$, $NiCO_3$), which include ions with different $3d$-state populations. Figure 2 shows the experimental scheme and the main results.

The blue curves were obtained in measurements below the resonance energy and illustrate the magnetic scattering intensity, which is symmetrical and insensitive to the phase of scattering. The red curves describe resonance and include a strong interference term, which breaks symmetry and specifies the phase of magnetic scattering (which reveals the sign of DMI). The experimental data (symbols) are indicated along with the fitting results (solid lines) calculated by the expression [27]

$$I(E,\psi,\eta) = f_m^2\sin^2\eta + |\Theta(E)|^2\cos^2 3\psi + 2\sigma_\varphi f_m|\Theta(E)|\cos 3\psi\sin\eta, \quad (1)$$

Table 1. Experimental and calculated angle of Dzyaloshinskii–Moriya deviation (in deg) and the number of electrons N_{3d} in the 3*d* orbitals in $FeBO_3$

Composition	Magnetic ion	N_{3d}	Canting angle of the moments of sublattices, deg (experiment)	Canting angle of the moments of sublattices, deg (calculation)
$FeBO_3$	Fe^{3+}	5.8	–0.9	–0.8

where f_m is the real positive quantity related to the nonresonance magnetic scattering amplitude, E is the X-ray energy, and $\Theta(E)$ is the complex expression related to the elastic X-ray resonance amplitude. For nonresonance data, we have $\Theta(E) = 0$ [27]. The calculations by Eq. (1) were carried out with the FDMNES software package for X-ray spectroscopy [30]. As follows from Eq. (1), the sign of DMI ($\sigma_\varphi = \pm$) can be determined by rotating a magnetic field at a retained fixed azimuth of the crystal ψ and X-ray energy E. The sign of the magnetic structure factor σ_φ is determined from the deviation of the measured intensity from $\eta = 90°$ or $\eta = 270°$ (red rings in Fig. 2 go up or down, respectively). As is seen in Fig. 2, the sublattice angularity is negative in $FeBO_3$ and $MnCO_3$ and is positive in $CoCO_3$ and $NiCO_3$.

The canting angle given in Table 1was calculated in the local density approximation with allowance for Coulomb interaction U and spin–orbit coupling SOC (LDA + U + SO) [27] in terms of the VASP software package [31, 32]. The calculation is seen to reproduce the experimentally detected sign and magnitude of DMI in $FeBO_3$. It should be noted that, for the $FeBO_3$ insulator, the calculation showed an ion–covalent bond rather than a purely ionic chemical bond.

3. MAGNETIC ANISOTROPY OF $FeBO_3$

3.1. Weak Ferromagnetism along the Threefold Axis and the Basal Anisotropy Induced by DMI and the Cubic Electric Field of $FeBO_3$ Crystal [33]

$FeBO_3$ crystals are a convenient object for revealing and studying new magnetic effects (as a rule, using anisotropic interaction parameters). The basal anisotropy and the weak ferromagnetic moment along the threefold axis in $FeBO_3$ were calculated in [33]. The free energy of an $FeBO_3$ crystal can be written as

$$\Phi = \left[\frac{1}{2}B\mathbf{M}^2 + \frac{1}{2}a\cos^2\theta + d_{DM}(L_xM_y - L_yM_x) + q\sin^3\theta\cos\theta\cos 3\varphi + tM_z\sin^3\theta\sin 3\varphi\right], \quad (2)$$

here, the following standard designations of antiferromagnetism and ferromagnetism vectors are used:

$$\mathbf{L} = (\mathbf{M}_1 - \mathbf{M}_2)/M,$$
$$\mathbf{M} = (\mathbf{M}_1 + \mathbf{M}_2)/M,$$
$$M = 2|\mathbf{M}_1| = 2|\mathbf{M}_2| = Ng\beta sB_{5/2}(x).$$

Here, B is the exchange interaction parameter expressed in the units of a magnetic field and θ and φ are the polar and azimuth angles of the antiferromagnetism vector, respectively.

The first term in Eq. (2) represents the exchange energy; the second and third terms describe the uniaxial anisotropy and the DMI, respectively; and the last two terms describe the basal anisotropy energy. Although the crystal structure of $FeBO_3$ is relatively simple, the behavior of the magnetic system during the rotation of the antiferromagnetism vector in the (111) plane when the last two terms in Eq. (2) are taken into account is relatively complex. In particular, this statement follows from the electron paramagnetic resonance (EPR) data [34], which demonstrate the effective distribution of the cubic crystal field axes in the $MBO_3 + Fe^{3+}$ (M = Ga, In, Sc, Lu) lattice (see also Fig. 3 in [33]).

The minimization of free energy (2) leads to the following expressions for the basal anisotropy and the weak ferromagnetic moment along the threefold axis, respectively:

$$E_q\sin^6\theta\cos 6\varphi = -\frac{(qM)^2}{4M(a + d_{DM}^2/B)}\sin^6\theta\cos 6\varphi,$$

$$M_z = -\frac{tM}{B}\sin^3\theta\sin 3\varphi.$$

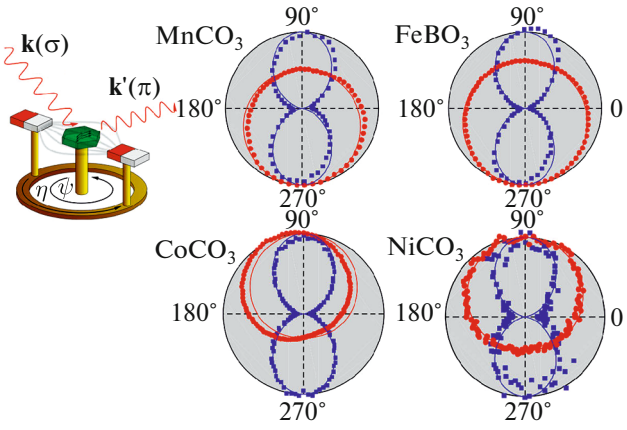

Fig. 2. (Color online) Schematic diagram of the X-ray diffraction experiment (scheme and main results). Normalized experimental diffraction intensities vs. η, which is the angle of magnet rotation about the c axis of the crystal. (thin solid lines) Fitting (borrowed from [27]).

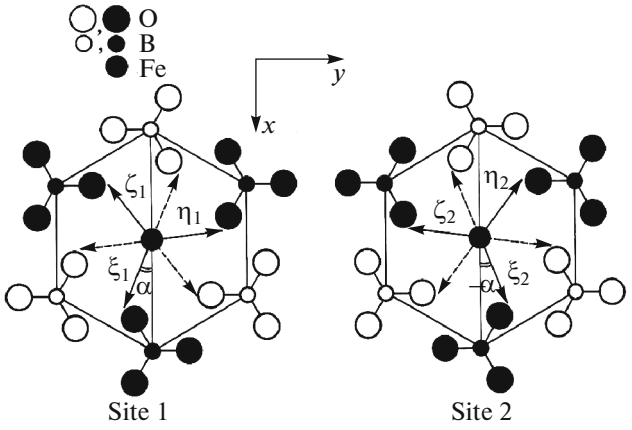

Fig. 3. Schematic distribution of the axes of cubic crystal field for the two nonequivalent sites of M^{3+} ions in the MBO_3 lattice. Black BO_3^{3-} ions are above the figure plane and white BO_3^{3-} ions are below the figure plane (borrowed from [15]).

To calculate "microscopic" expressions for the basal hexagonal and the weak ferromagnetic moment along the threefold axis, we write the following Hamiltonian to take into account two nonequivalent sites of Fe^{3+} ions in the $FeBO_3$ lattice [33]:

$$\hat{H} = g\beta\mathbf{H}_j^{\text{eff}}\mathbf{s}_j + \frac{1}{3}D_{cf}O_{2j}^0 + \frac{F_{cf}}{180}O_{4j}^0 - \frac{a_{cf}}{180}[O_{4j}^0 - 20\sqrt{2}(O_{4j}^3\cos 3\alpha_{cfj} - \tilde{O}_{4j}^3\sin 3\alpha_{cfj})] + d_{DM}(s_{x1}s_{y2} - s_{y1}s_{x2}), \quad (3)$$

where the first term of the exchange interaction is written in the molecular field approximation; $\mathbf{s}_j$ is the operator of the spin of the jth ion; D_{cf}, F_{cf}, and a_{cf} are axial and cubic constants, respectively; O_{nj}^m are the equivalent spin operators, the form and matrix elements of which are given in, e.g., [35]; and the second, third, and fourth (for Hamiltonian constant a_{cf}) terms describe the interactions of the axial and cubic symmetry, respectively. The last term describes DMI. In Eq. (3), a_{cfi} is the angle between the projections of the cubic crystal field axes and the projections of the planes of symmetry of the crystal onto the (111) plane at jth sites 1 and 2 (some planes of symmetry of the crystal are indicated by thin solid lines in Fig. 3). This distribution of the cubic crystal field axes follows from EPR experiments on isostructural diamagnetic analogs with an Fe^{3+} impurity [34]. Note that the cubic crystal field axes are taken to be crystallographically preferred equivalent directions characterized by certain symmetry and physical properties. These directions can be determined, in particular, by X-ray diffraction.

The eigenvalues of Eq. (3) were obtained by the perturbation theory. The expressions for energy levels were used to calculate the values and temperature dependences of the basal magnetic anisotropy and the weak ferromagnetic moment along the threefold axis. The effective field for the basal magnetic anisotropy has the form [33]

$$H_{qcfDM}\sin^6\theta\cos 6\varphi = -\frac{a_{cf}^2\{[r(Y)/s]^2[|H_{DM}(0)|/H^{\text{eff}}(0)]\sin 3\alpha_{cf} - (1/3)\cos 3\alpha_{cf}\}^2}{2\{H_A(0) + H_{DM}^2(0)/H_E(0)\}B_{5/2}^3(x)}\sin^6\theta\cos 6\varphi.$$

Here,

$$r(Y) = \frac{5}{2}\frac{z_2}{z_0} = \frac{5}{2}\frac{-Y^5 + 3Y^4 - 2Y^3 - 2Y^2 + 3Y - 1}{Y^5 + Y^4 + Y^3 + Y^2 + Y + 1}$$

is the function [36] introduced to calculate the single-ion magnetic anisotropy of a cubic crystal, $H^{\text{eff}}(0\text{ K}) = (1/2)H_E(0\text{ K})$ is the exchange field (3×10^6 Oe), $H_{DM} = 10^5$ Oe is the Dzyaloshinskii–Moriya field at $T = 0$ K [37], $\alpha_{cf} = 24°$, $a_{cf} = 130$ Oe, and $B_{5/2}(x)$ is the Brillouin function for a spin of 5/2. The magnetic moment calculated along the threefold axis per mole of an $FeBO_3$ crystal is

$$\sigma_z(T) = -\sqrt{2}Ng\beta sB_{5/2}(x)\frac{a_{cf}|H_{DM}|}{2(H^{\text{eff}})^2} \times \frac{r(Y)}{sB_{5/2}(x)}\cos 3\alpha_{cf}\sin^3\theta\sin 3\varphi.$$

From here on, we have $\alpha_{cf1} = \alpha_{cf} = \alpha$ for $j = 1$ and $\alpha_{cf2} = -\alpha_{cf} = -\alpha$ for $j = 2$ (see Fig. 3). The hexagonal anisotropy determined by Fe^{3+} ions in $FeBO_3$ with allowance for two mechanisms is estimated at $H_{qcfDM}(0\text{ K}) = -1.0 \times 10^{-2}$ Oe (according to EPR data), and the experimental value is $H_q(0\text{ K}) = -1.1 \times 10^{-2}$ Oe (according to antiferromagnetic resonance data).

The experimental value of σ_z obtained for $FeBO_3$ crystals is 1.3×10^{-3} G cm^3/g [38]. This estimation was carried out at $T = 77$ K using the results from [9]. The theoretical estimate [39] caused by the introduction of Fe^{3+} ions at $T = 0$ K gives 2.4×10^{-3} G cm^3/g at constants $a_{cfmc} = 130$ Oe and $\alpha_{cfmc} = 24°$ [15].

The authors of [40] considered the possibility of experimental observation of the fact that the magnetic moments of iron leave the basal plane by comparing the theory of spin waves with NMR and Mössbauer spectra. The application of rotation magnetometry to rhombohedral weak ferromagnets [38] allowed a periodic change to be detected in the magnetic moment along axis c $M_c = AM_s\cos(3\psi)$, where ψ reflects the rotation of a magnetic field in the basal plane about one of the threefold axes and M_s is the weak spontaneous magnetic moment. The measurements performed on a few α-Fe_2O_3 single crystals and one $FeBO_3$ single crystal showed that the angle of inclination of magnetic moments to axis c is about 10^{-7} rad. Parameter A in the ferroborate is lower than that in hematite by a factor of 2–3.

Note that one angular constant α_{cf} is sufficient to describe weak ferromagnetic moment σ_z along axis c_3, which was calculated in the second approximation of the perturbation theory. For example, apart from the cubic electric field, the weak ferromagnetic moment along c_3 includes the DMI-induced contribution. As a result, angle α_{cf}, which enters into the σ_z expression, corresponds to angle $60° - \alpha_{cf}$ in Fig. 3 and, with allowance for the threefold axis, angle $3(60° - \alpha_{cf})$. Then, we have $\cos[3(60° - \alpha_{cf})] = -\cos3\alpha_{cf}$, which corresponds to the sign and magnitude of the σ_z expression.

3.2. Surface Magnetic Anisotropy in Iron Borate

Breaking the symmetry of the environment of paramagnetic ions in the surface layer of a magnetic crystal causes a number of phenomena, including the appearance of surface magnetic anisotropy predicted by Néel [41]. However, surface anisotropy had not been experimentally detected for a long time because of its smallness in most compounds. Favorable conditions for its detection appeared during the investigation of weak ferromagnets with an easy-plane anisotropy due to a low demagnetizing field because of a low resulting magnetic moment and the absence (or low value) of anisotropy in the basal plane; against this background, the manifestation of surface anisotropy turned out to be more pronounced. The authors of [42] were likely to be the first to detect surface anisotropy when studying the transverse Kerr effect during the reflection of a light beam from the (111) basal plane of a hematite crystal. Later, analogous measurements were carried out on rare-earth orthoferrites [43] and $FeBO_3$ [44]. In the next works (see, e.g., [45]), researchers comprehensively studied the nature of surface anisotropy. For example, the theory of surface magnetism of the $FeBO_3$ iron borate was extended with allowance for the contribution of breaking the symmetry of the crystal field to the anisotropy energy [46]. For this purpose, a model of a distorted oxygen octahedron with iron ions in the near-surface layer of the $(10\bar{1}4)$ crystal face was considered. The contribution of the crystal field to the surface magnetic anisotropy was calculated using the perturbation theory. The calculations demonstrate that iron environment distortions bring about a significant contribution of the crystal field to the surface magnetic anisotropy. As follows from the dipole contribution [47], the surface magnetic anisotropy can be described on the assumption of 1% distortions in the near-surface layer. Surface energy density σ (here, for the $(10\bar{1}4)$ face) includes the contributions of dipole ($\sigma_{dip} = a_{Sdip}\sin^2\varphi$ [47]) and crystal field [46]. The distortions of the oxygen environment of lattice ions, which are taken into account in the general form, give rise to the surface magnetic anisotropy $\sigma_{cf} = -10NB_{2S}^2\sin^2\varphi = a_{Scf}\sin^2\varphi$. Here, $N = 6.0036 \times 10^{18}$ m^{-2} is the number of Fe^{3+} ions per unit surface on the $(10\bar{1}4)$ face and B_{2S}^2 is the spin Hamiltonian constant. The total surface magnetic anisotropy constant can be written as $a_S = a_{Sdip} + a_{Scf}$, where the components depend on relative distortion $\varepsilon = \Delta a_r/a_r$ (a_r is the rhombohedral cell edge length). The authors of [46] found that the effective field on the $(10\bar{1}4)$ face at 300 K ($H_c = 1$ kOe) is much higher than the field (0.2 kOe) calculated without regard for the lattice distortions in the near-surface layer.

4. EXTREMAL INSTABILITY OF THE MAGNETOELASTIC EXCITATIONS IN $FeBO_3$ SINGLE CRYSTAL

Iron borate exhibits a strong magnetoelastic linear interaction [48, 49]. The nonlinear magnetoelastic excitations in an $FeBO_3$ crystal were experimentally and theoretically studied [50, 51]. The acoustic excitations in antiferromagnetic crystals with an easy-plane anisotropy, including $FeBO_3$, occur in the form of hybrid magnetoelastic waves, which are called quasi-phonons. The strong acoustic nonlinearity of such crystals creates possibilities for coupling a few quasi-phonons. Such coupled states, namely, three-quasi-phonon coupled excitations, were detected in a weak α-Fe_2O_3 ferromagnet during uniform radio-frequency pumping [51, 52]. Later, the coupling of three quasi-phonons was experimentally detected in an $FeBO_3$ crystal [50]. The theoretical analysis [50] revealed a number of specific dynamic characteristics, which distinguish three-phonon parametric coupling from the well-known parametric excitation of quasi-phonon pairs. In particular, this is the dependence of

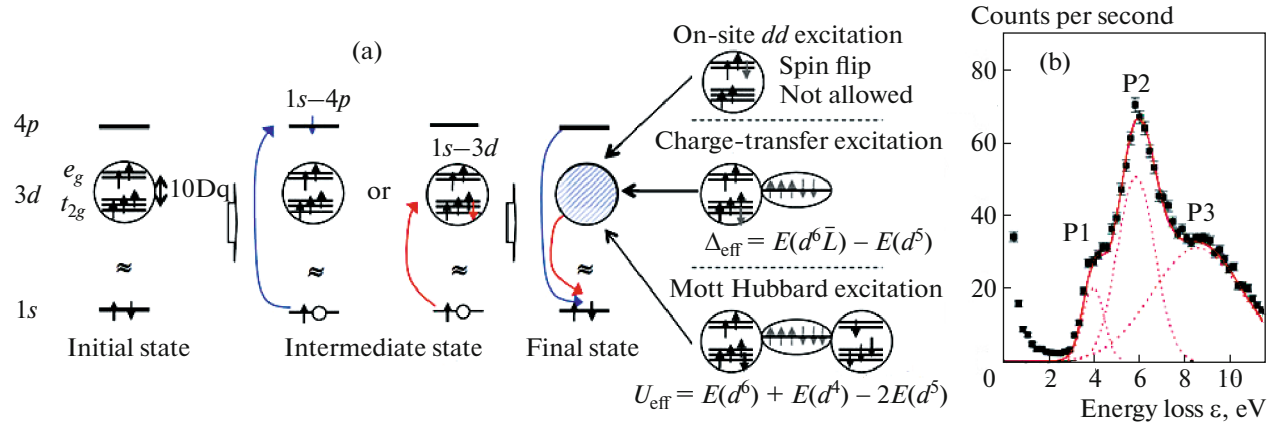

Fig. 4. (Color online) (a) Schematic diagram for the formation of the Fe *K* edge of RIXS. (b) Spectrum of pre-threshold specific features in $FeBO_3$ (borrowed from [21]).

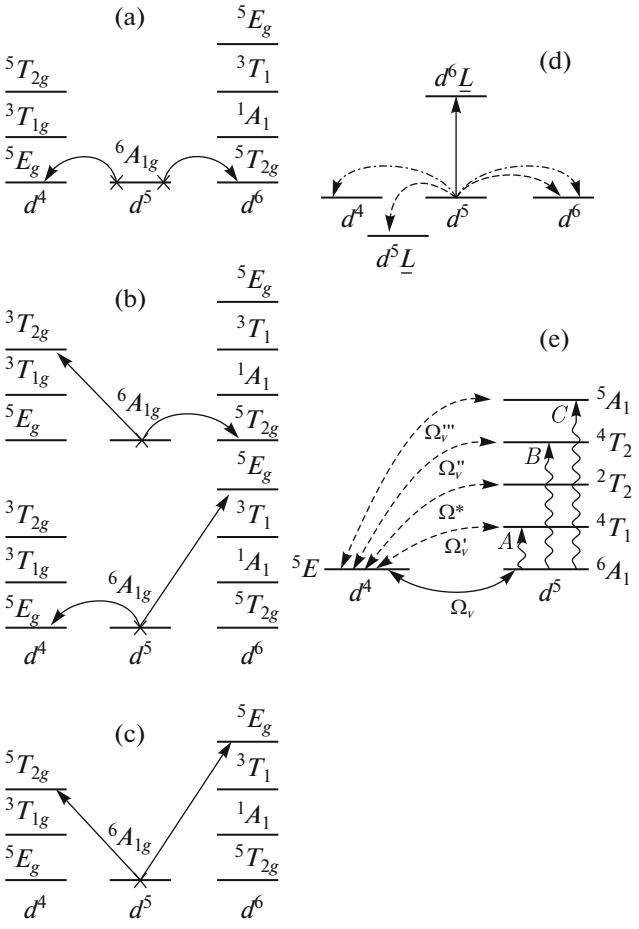

Fig. 5. Scheme of the many-electron excitations in $FeBO_3$. (a–c) Mott–Hubbard excitations $d_i^5 d_j^5 \leftrightarrow d_i^4 d_j^6$ associated with pre-threshold features P1, P2, and P3 in RIXS spectra. (d): (solid and dashed lines) Two types of charge-transfer excitations and (dot-and-dash lines) Mott–Hubbard excitations (borrowed from [21]). (e) Virtual one-electron states induced by excitations from unfilled d^4 term to unfilled excited d^5 terms (borrowed from [20]).

an instability threshold on both the pumping amplitude and the number of initial quasi-phonons, i.e., the amplitude of an initial magnetoelastic wave. The most substantial difference is an explosive increase in the number of quasi-phonons up to singularity of the coupled-wave amplitudes in a finite pumping time interval outside the instability threshold. The post-threshold amplification for traveling magnetoelastic waves was accompanied by spatial excitation localization. The post-threshold limitation of the excited-wave amplitudes was shown to be mainly caused by a nonlinear shift in the magnetoelastic mode frequencies. An explosive instability was reached when the nonlinear frequency shift was compensated by the quasi-singular modulation of the electromagnetic pumping field phase.

5. THEORETICAL AND EXPERIMENTAL MANIFESTATION OF THE MANY-ELECTRON EFFECTS IN THE ELECTRONIC STRUCTURE OF $FeBO_3$

As many 3*d* metal oxides, $FeBO_3$ crystals are Mott insulators due to strong Coulomb electron correlations inside the cation. The more exact Zaanen–Sawatzky–Allen classification [53] considers the following two types of competing excitations: Mott–Hubbard excitation with energy U and charge-transfer excitation energy E_{CT} (see Fig. 5d). The insulator gap is determined by the lowest energy between them: at $U < E_{CT}$, we have a Mott–Hubbard insulator; at $U > E_{CT}$, we have a charge-transfer insulator. Experimental information about these excitations in iron oxides can be obtained from the resonant inelastic X-ray scattering (RIXS) spectra of the Fe *K* edge [54–56]; these spectra for $FeBO_3$ were recorded in [21]. The schematic diagram of formation of the Fe *K* edge is shown in Fig. 4.

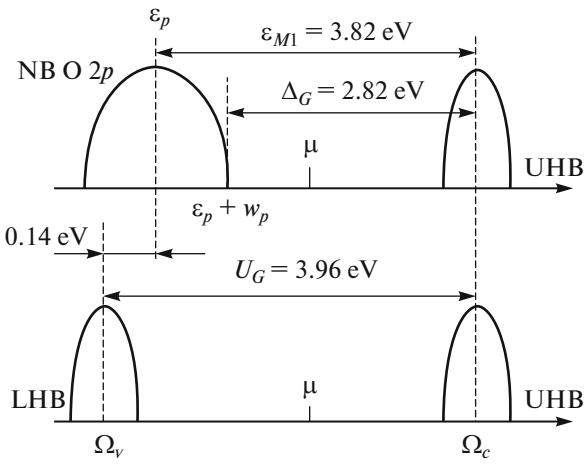

Fig. 6. Scheme of the electronic structure of $FeBO_3$ obtained from RIXS experiments. (top panel) Contributions of charge-transfer excitations and (bottom panel) contributions of Mott–Hubbard excitations (borrowed from [21]).

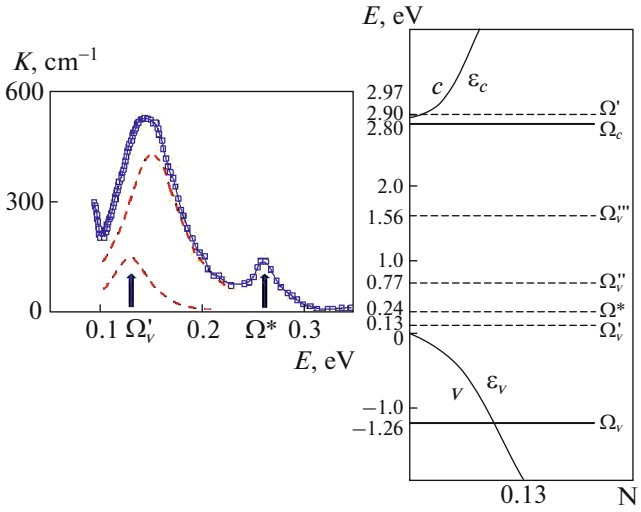

Fig. 7. (Color online) (a) IR room-temperature spectra of $FeBO_3$ and (b) density of single-particle states with indicated virtual levels (borrowed from [20]).

The Mott–Hubbard excitations (d–d transitions) are related to an electron jump from one cation to another: for the Fe^{3+} ion, this means the initial state $d_i^5 d_j^5$ and the final state $d_i^4 d_j^6$. The crosses in Figs. 5a–5c indicate the only high-spin state occupied at zero temperature $^6A_1$. Excitations into the final states of terms d_i^4 and d_j^6 are only possible from this state. It should be noted that a large number of excited terms in the final states leads to various Mott–Hubbard excitation energies, which are visible in RIXS spectra below the threshold (Fig. 4b). The Mott–Hubbard excitations and the charge-transfer excitations in $FeBO_3$ were described in detail in [21]. Figure 6 shows the scheme of the density of states in $FeBO_3$, which was obtained in terms of the generalized tight-binding (GTB) method [19, 57]. As follows from this scheme, $FeBO_3$ is a charge-transfer insulator: the valence band top is determined by the p states of oxygen, and the conduction band bottom is determined by the d states of iron. The insulator gap is smaller than the charge-transfer gap by the half-width of the p band and the half-width of the upper Hubbard band (UHB). Here, the centers of gravity of the lower (LHB) and upper (UHB) bands are determined by the energies

$$\begin{aligned} \Omega_v &= E(d^5, {}^6A_1) - E(d^4, {}^5E), \\ \Omega_c &= E(d^6, {}^5T_2) - E(d^5, {}^6A_1). \end{aligned} \quad (4)$$

Figure 5e shows the excitations that form LHB: these are single-particle excitations (quasiparticles) between filled ground state d^5 and unfilled ground state d^4. The spectral weight of such a quasiparticle is the sum of the occupation numbers of the initial and final states (in our case, 1). Figure 5e also depicts unusual single-particle excitations from unfilled ground state d^4 to unfilled excited d^5 states with a zero spectral weight, i.e., the so-called virtual states predicted in the GTB theory for doped cuprates [23]. As is shown by the vertical wavy lines in Fig. 5e, optical pumping A, B, and C of the excited terms of Fe^{3+} ions leads to nonzero occupation numbers of these terms and to nonzero spectral weight of quasiparticles with energies Ω'_v, Ω^*, Ω''_v, and Ω'''_v. Such optically induced quasiparticles were detected in the IR absorption spectra of $FeBO_3$ single crystals (Fig. 7) [20].

An intense IR absorption line is shown in Fig. 7a with decomposition into two Lorentzian lines with energies of 0.15 eV (E_g phonon at 1210 cm^{-1} [58]) and 0.13 eV (electron excitation Ω'_v). The density of states in Fig. 7b refines the rough picture obtained from RIVX and shown in Fig. 6: LHB and UHB are present, and the valence band top lies above LHB and determines a charge-transfer insulator gap. The virtual states indicated by primes do not contribute to the density of states when a sample in the ground state and make a nonzero contribution in an optically excited state.

6. CHANGES IN THE ELECTRONIC AND MAGNETIC PROPERTIES OF $FeBO_3$ AT HIGH PRESSURES

When the lattice parameters change because of an applied pressure, all parameters that depend on the interatomic distance and determine the electronic structure also change. For Mott–Hubbard insulators, the most important changing parameters are the crystal field (10Dq in the case of isotropic compression) and the interatomic electron jump parameters. The

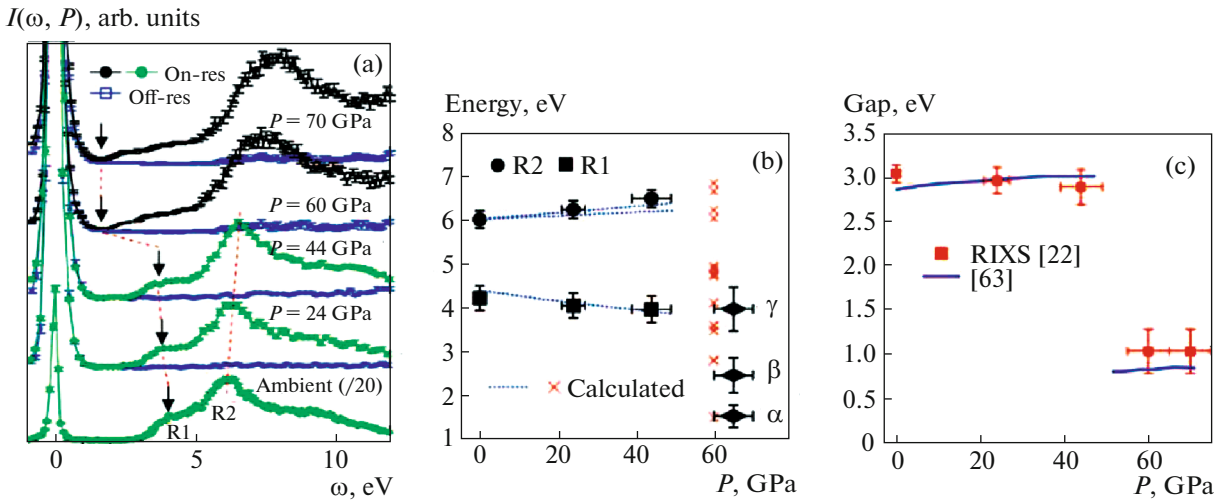

Fig. 8. (Color online) (a) Pressure-induced changes in RIXS spectra indicating changes in the insulator gap (arrows), (b) Mott–Hubbard excitation energies calculated from these spectra, and (c) insulator gap determined from RIXS data and optical absorption spectra [63] (borrowed from [22]).

first parameter determines the competition between the high-spin (HS) and low-spin (LS) terms of ions d^n. When the decrease in the HS energy induced by the intraatomic Hund exchange interaction becomes smaller than the increase in the crystal field energy when pressure increases, the crossover of the HS and LS states (i.e., intersection of their energy levels) takes place for ions with $n = 4–7$ [59, 60].

The experimental investigations of the high-pressure properties of $FeBO_3$ in chambers with diamond anvils revealed an isostructural transition [61] and the collapse of its magnetic moment according to Mössbauer spectroscopy data [62, 63] at room temperature at a pressure $P_c = 47$ GPa. At the crossover point, the insulator gap changes jumpwise and the absorption spectrum also changes [63], which indicates changes in the electronic structure. The experimental data available until 2009 were reviewed in [17]. Below, we present some additional data appeared after review [17]. Figure 8 shows the RIXS spectra of $FeBO_3$ recorded at high pressures [22]; they demonstrate changes in the electronic structure. The insulator gap obtained from these data as a function of pressure coincides with the data obtained from absorption spectra recorded at high pressures [63] (see Fig. 8c).

Intraatomic Coulomb parameter $U = E(0) + E(2) - 2E(1)$ is known for the Hubbard model with one orbital and three $E(n)$ terms for $n = 0, 1, 2$. Effective Hubbard parameter $U_{\text{eff}} = E(n-1) + E(n+1) - 2E(n)$ can also be introduced for multiorbital Mott–Hubbard models of insulators with ionic configuration d^n. This parameter includes the energies of the ground terms for d^n configurations; since these terms change at the spin crossover, parameter U_{eff} changes jumpwise. This jump for $FeBO_3$ is not small, from 4.2 eV for the HS state to 1.4 eV in the LS state [63]. When pressure increases further, both the electronic and magnetic properties change in the LS region [64] (Fig. 9). A decrease in U_{eff} gradually suppresses the charge-transfer gap via a decrease in the UHB energy Ω_c (Fig. 9a). The charge-transfer gap then vanishes at a pressure $P_m > P_c$ (Fig. 9b). As a result, all properties of $FeBO_3$ are thought to undergo radical changes: a metal with a variable valence, which is described by the periodic Anderson model, is expected instead of a Mott–Hubbard insulator. Such structures are often called Kondo lattices (Fig. 9c). Metals with a variable cation valence can exhibit superconductivity below critical temperature T_c similarly to the superconductivity of heavy fermions. Extrapolating the pressure dependence of the insulator gap, the authors of [65] estimated the semiconductor–metal transition point at $P_m = 210$ GPa.

Direct measurements of the electrical properties of $FeBO_3$ were performed by the four-probe method in a cell with diamond anvils over wide pressure (up to 198 GPa) and temperature (4.2–300 K) ranges [66]. Figure 10 shows the electrical resistance as a function of pressure. In the HS region at $P < 46$ GPa, the electrical resistance even at $T = 300$ K is so high that it cannot be measured; measurements are only possible in the LS state. The following three characteristic pressure ranges can be distinguished in Fig. 10a: (i) rapid decrease in the electrical resistance in the pressure range 46–100 GPa, (ii) exponential decrease in the electrical resistance in the range 100–160 GPa, and (iii) saturation in the range 160–198 GPa. Both the resistance and the activation energy at room temperature decrease, and this energy reaches 0.1 eV at the highest pressure (Fig. 10b). The temperature dependences of the electrical resistance to a pressure of

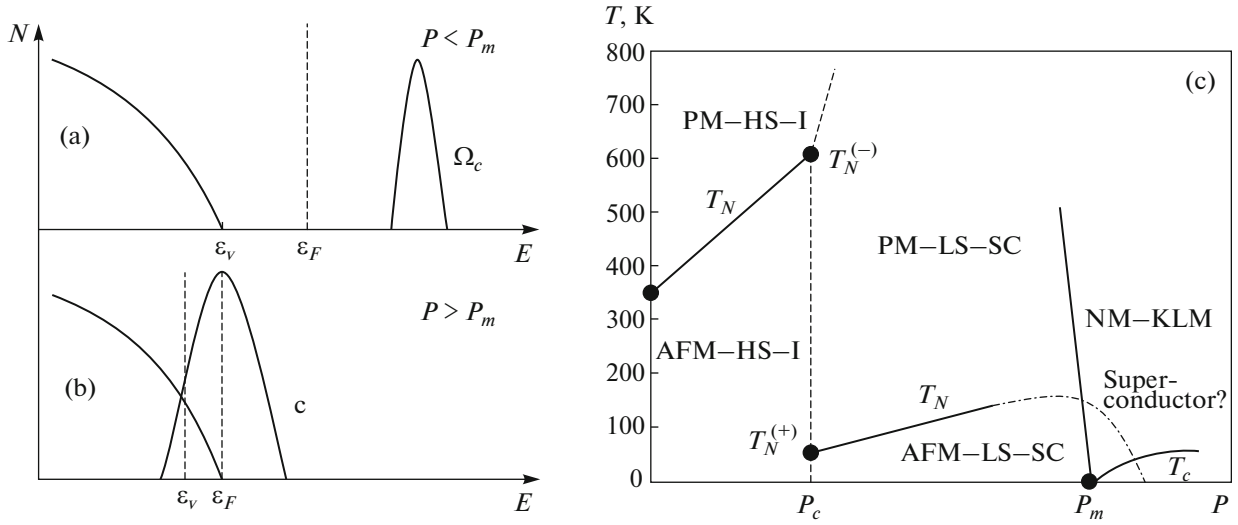

Fig. 9. (a) Fragment of the density of states in $FeBO_3$ with indicated charge-transfer gap, which vanishes at point P_m (b). (c) Phase diagram with regions of an HS insulator (HS-I) below P_c and an LS semiconductor (LS-SC) in the range $P_c < P < P_m$, which can be in both antiferromagnetic (AFM) and paramagnetic (PM) states, and nonmagnetic metallic state of the Kondo lattice (NM-KLM) above P_m with possible superconductivity (SC) below T_c (borrowed from [64]).

100 GPa are described by a conventional activation Arrhenius law; at higher pressures, the deviations from the activation law become stronger at low temperatures (Fig. 11a). These deviations are clearly visible in the inset to Fig. 11a at a pressure of 163 GPa, where measurements were carried out to the liquid-helium temperature. When analyzing the temperature dependences of the resistance at high pressures, we plotted the activation energy as a function of temperature (Fig. 11b). The activation energy at a pressure of 163 GPa tends toward zero at zero temperature. To understand these results, we recall the transition into a metallic state at point P_m, which was predicted in the phase diagram in Fig. 9c. The estimate given above ($P_m = 210$ GPa) was obtained in [65], where the pressure dependence of the activation energy was measured up to 140 GPa and was rather inaccurately extrapolated. The later data of this team [66] were obtained up to 198 GPa; therefore, the data in Fig. 11b and a value $P_m = 163$ GPa are more reliable. As is shown in Fig. 9b, d-level energy Ω falls inside p band ε_v at $P > P_m$; in this situation, the periodic Anderson model is more adequate. Due to the p–d hybridization with parameter V_{pd}, two electron bands

$$E^{\pm} = \frac{1}{2}\left[\Omega + \varepsilon_v \pm \sqrt{(\Omega - \varepsilon_v)^2 + \tilde{V}_{pd}^2}\right], \qquad (5)$$

separated by the hybridized gap

$$E_g = E^{+} - E^{-} = \sqrt{(\Omega - \varepsilon_v)^2 + \tilde{V}_{pd}^2} \qquad (6)$$

form. Here, the hybridization parameter in the magnetically ordered phase is renormalized,

$$\tilde{V}_{pd} = V_{pd}(1 \pm \langle S^z \rangle / S). \qquad (7)$$

In Eq. (7), the ferromagnetic phase undergoes spin projection splitting [67] and the antiferromagnetic phase undergoes sublattice splitting [68]. In any case, the renormalized hybridization parameter at zero temperature vanishes for either one spin subband in the ferromagnetic phase or one sublattice in the antiferromagnetic phase. Therefore, the insulator gap vanishes at zero temperature and degeneracy point $\Omega = \varepsilon_v$. This unusual $FeBO_3$ metallization mechanism at a low temperature was likely to be observed at pressures above 163 GPa [66].

Note that the experimental data on the magnetic order in $FeBO_3$ at high pressures in the LS region are rather scarce. The authors of [64] give only two points for the Néel temperature in the LS state, which were determined from the effective field measured in the Mössbauer effect. This method gives information only on the local magnetic field at a nucleus and cannot be used to separate ferromagnetic and antiferromagnetic states. The conclusion regarding the antiferromagnetic LS state in the phase diagram in Fig. 9c was made on the assumption that the spin crossover only changes the spin ($5/2 \leftrightarrow 1/2$) and does not change the character of antiferromagnetic interaction. Using the recently developed orbital-selective method for calculating the superexchange interaction in Mott–Hubbard insulators [69], the authors of [70] showed that the exchange interaction in $FeBO_3$ is antiferromagnetic in the HS state and changes its sign in the LS state and becomes ferromagnetic. This behavior is related to another set of d orbitals involved in the formation of superexchange interaction through oxygen ions. Thus, the question of the character of magnetic

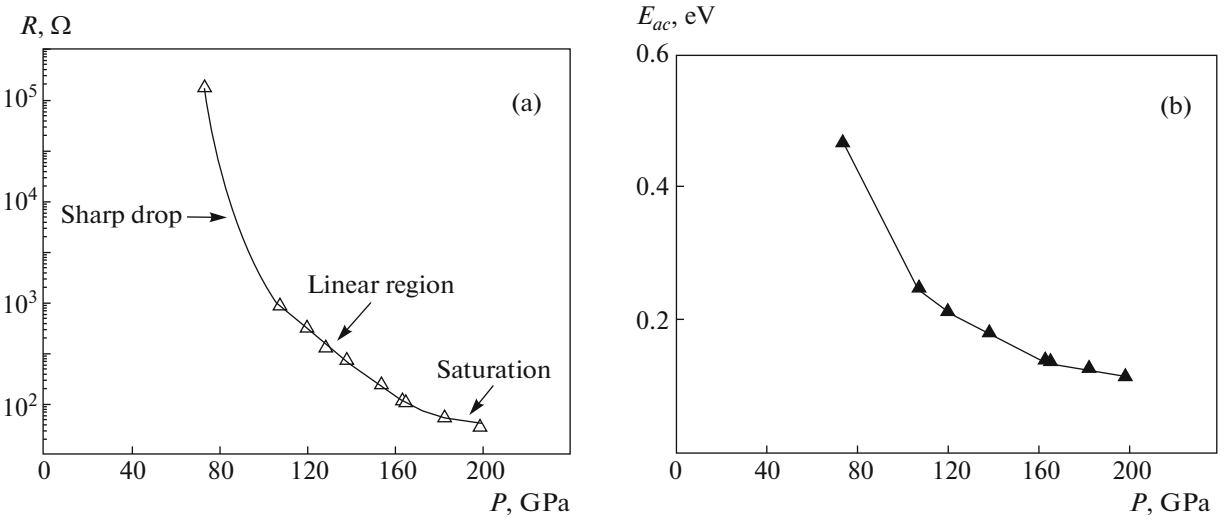

Fig. 10. Pressure dependences of (a) electrical resistance of $FeBO_3$ single crystal and (b) activation energy at $T = 300$ K (borrowed from [66]).

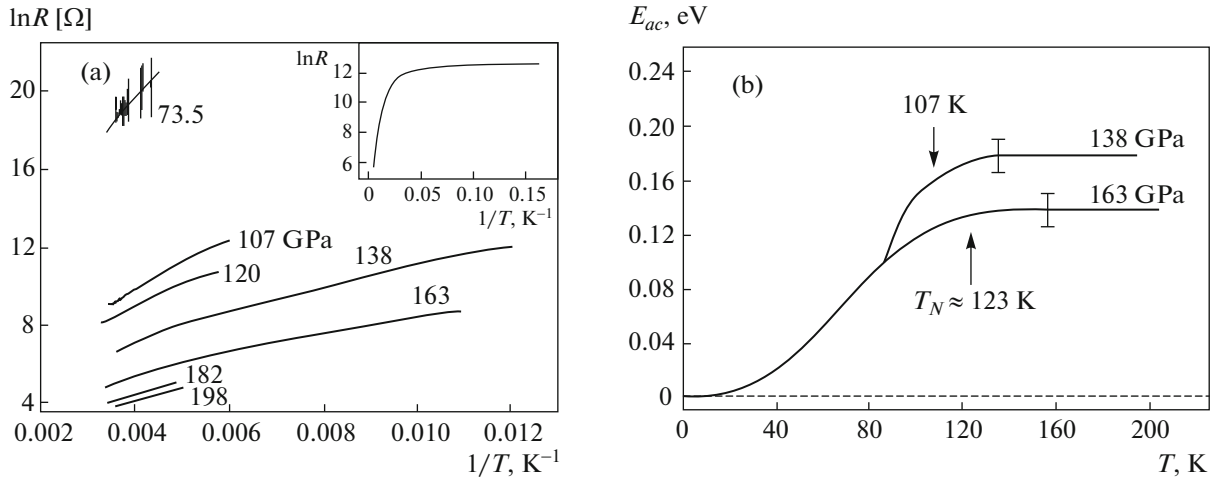

Fig. 11. (a) Logarithm of the electrical resistance of $FeBO_3$ vs. reciprocal temperature at various pressures; (inset) dependence up to $P = 163$ GPa. (b) Temperature dependences of the activation energy at pressures of 138 and 163 GPa. The arrows indicate the magnetic ordering temperatures calculated from the phase diagram shown in Fig. 9c (borrowed from [66]).

order in $FeBO_3$ at pressures higher than 50 GPa is still open and is to be experimentally verified.

The sign of exchange interaction changes during the optical pumping of *d*–*d* transitions due to the same cause. The authors of [70] showed that a pair of the nearest neighbors of Fe^{3+} ions in the ground state has an antiferromagnetic exchange; however, if one of the ions is excited into term $^4T_2$ (which corresponds to the *B* band in the absorption spectrum), its interaction with the neighboring unexcited spin becomes ferromagnetic. This optically induced change in the sign of exchange interaction is likely to cause the unusual phenomena observed in femtosecond magnetooptics [16, 71–73]. The relation between the changes in the exchange interaction at spin crossovers at high pressures and during optical excitation due to *d*–*d* transitions was recently discussed [74]. During optical pumping in the *B* band in the absorption spectrum, the Fe^{3+} ion comes from an HS state with $S = 5/2$ to an intermediate-spin state with $S = 3/2$, which can be considered as a dynamic spin crossover. In this case, other *d* orbitals are populated and the character of covalent bond changes (e.g., weak π bond appears instead of strong e_g bond).

ACKNOWLEDGMENTS

We thank I.S. Lyubutin, A.G. Gavrilyuk, I.A. Troyan, and A.M. Vorotynov for the long-term useful cooperation in studying the properties of ferroborates; R.V. Pisarev,

A.V. Kimel', A.M. Kalashnikova, and R.V. Mikhailovskii for the helpful discussions of the problems of ultrafast magnetism and femtosecond optics; and L.M. Rudenko for the technical assistance.

FUNDING

This work was supported by the Russian Science Foundation, project no. 18-12-00022.

ADDITIONAL INFORMATION

This article was prepared for the special issue dedicated to the centenary of A.S. Borovik-Romanov.

REFERENCES

1. A. S. Borovik-Romanov and M. P. Orlova, Sov. Phys. JETP **4**, 531 (1956).
2. A. S. Borovik-Romanov, Sov. Phys. JETP **9**, 539 (1959).
3. A. S. Borovik-Romanov and E. G. Rudashevskii, Sov. Phys. JETP **20**, 1407 (1964).
4. A. S. Borovik-Romanov, in *Problems of Magnetism, Collection of Articles* (Nauka, Moscow, 1972), p. 47 [in Russian].
5. I. Bernal, C. W. Struck, and J. G. White, Acta Crystallogr. **16**, 849 (1963).
6. V. V. Rudenko, V. N. Seleznev, and R. P. Smolin, in *Proceedings of the 4th All-Union Workshop on Crystal Growth, Erevan, 1972*, p. 149.
7. L. V. Velikov, E. G. Rudashevskii, and V. N. Seleznev, Izv. Akad. Nauk SSSR **36**, 1531 (1972).
8. L. V. Velikov, A. S. Prokhorov, E. G. Rudashevskii, and V. N. Seleznev, JETP Lett. **15**, 511 (1972).
9. A. M. Kadomtseva, R. Z. Levitin, Yu. F. Popov, V. V. Uskov, and V. N. Seleznev, Sov. Phys. Solid State **14**, 172 (1972).
10. R. Diehl, A. Raubar, and F. Friedrich, J. Cryst. Growth **29**, 225 (1975).
11. L. N. Bezmaternykh, V. G. Mashchenko, V. A. Chikhachev, and V. S. Bliznyakov, Inventor's Certificate No. 1059029 (1983).
12. S. G. Ovchinnikov and V. V. Rudenko, J. Cryst. Growth **455**, 55 (2016).
13. S. Yagupov, M. Strugatsky, K. Seleznyova, et al., Cryst. Growth Des. **18**, 7435 (2018).
14. S. Yagupov, M. Strugatsky, K. Seleznyova, et al., J. Magn. Magn. Mater. **417**, 338 (2016).
15. S. G. Ovchinnikov and V. V. Rudenko, Phys. Usp. **57**, 1180 (2014).
16. A. Kirilyuk, A. V. Kimel, and T. Rasing, Rev. Mod. Phys. **82**, 2731 (2010).
17. I. S. Lyubutin and A. G. Gavriliuk, Phys. Usp. **52**, 989 (2009).
18. V. E. Dmitrienko, E. N. Ovchinnikova, S. P. Collins, et al., Nat. Phys. **10**, 202 (2014).
19. S. G. Ovchinnikov and V. N. Zabluda, J. Exp. Theor. Phys. **98**, 135 (2004).
20. S. G. Ovchinnikov, B. A. Gizhevskii, N. V. Kazak, V. V. Rudenko, and A. V. Telegin, JETP Lett. **90**, 519 (2009).
21. J. Kim, Yu. Shvyd'ko, and S. G. Ovchinnikov, Phys. Rev. B **83**, 235109 (2011).
22. J. Kim, V. V. Struzhkin, S. G. Ovchinnikov, Yu. Orlov, et al., Europhys. Lett. **108**, 37001 (2014).
23. V. A. Gavrichkov, S. G. Ovchinnikov, A. A. Borisov, and E. V. Goryachev, J. Exp. Theor. Phys. **91**, 369 (2000).
24. S. G. Ovchinnikov, JETP Lett. **77**, 676 (2003).
25. M. M. Korshunov, V. A. Gavrichkov, S. G. Ovchinnikov, et al., Phys. Rev. B **72**, 165104 (2005).
26. M. M. Korshunov, S. G. Ovchinnikov, E. I. Shneyder, et al., Mod. Phys. Lett. B **26**, 1230016 (2012).
27. G. Beutier, S. P. Collins, O. V. Dmitrova, et al., Phys. Rev. Lett. **119**, 167201 (2017).
28. A. S. Borovik-Romanov, in *Results of Science, Collection of Articles* (Akad. Nauk SSSR, Moscow, 1962), p. 7 [in Russian].
29. E. A. Turov, *Physical Properties of Magnetically Ordered Crystals* (Akad. Nauk SSSR, Moscow, 1963), p. 224 [in Russian].
30. Y. Joly, O. Bunau, J. E. Lorenzo, et al., J. Phys.: Conf. Ser. **190**, 012007 (2009).
31. G. Kresse and J. Hafner, Phys. Rev. B **47**, 558 (1993).
32. G. Kresse and J. Furthmüller, Phys. Rev. B **54**, 11169 (1996).
33. S. G. Ovchinnikov, V. V. Rudenko, and A. M. Vorotynov, J. Exp. Theor. Phys. **128**, 443 (2019).
34. C. N. Lukin, V. V. Rudenko, V. N. Seleznev, et al., Sov. Phys. Solid State **22**, 29 (1980).
35. S. A. Al'tshuler and B. M. Kozyrev, *Electron Paramagnetic Resonance in Compounds of Transition Elements* (Wiley, New York, 1974; Nauka, Moscow, 1972).
36. W. P. Wolf, Phys. Rev. **108**, 1152 (1957).
37. V. G. Bar'yakhtar, V. D. Doroshev, N. M. Kovtun, et al., in *Proceedings of the 19th All-Union Workshop on Low Temperature Physics Minsk, 1976*, p. 80.
38. P. J. Flanders, J. Appl. Phys. **43**, 2430 (1972).
39. S. G. Ovchinnikov, V. V. Rudenko, and V. I. Tugarinov, Phys. Solid State **58**, 1995 (2016).
40. M. Eibschutz and M. E. Lines, Phys. Rev. B **7**, 4907 (1973).
41. L. Neel, J. Phys. Radium **15**, 225 (1954).
42. G. S. Krinchik, A. P. Khrebtov, A. A. Askochenskii, and V. E. Zubov, JETP Lett. **17**, 335 (1973).
43. E. A. Balykina, E. A. Gan'shina, and G. S. Krinchik, Sov. Phys. JETP **66**, 1073 (1987).
44. V. E. Zubov, G. S. Krinchik, V. N. Seleznev, and M. B. Strugatskii, Sov. Phys. JETP **67**, 2122 (1988).
45. E. M. Maksimova, I. A. Nauhatsky, M. B. Strugatsky, and V. E. Zubov, J. Magn. Magn. Mater. **322**, 477 (2010).
46. M. Strugatsky, K. Seleznyova, V. Zubov, et al., Surf. Sci. **668**, 80 (2018).
47. V. E. Zubov, G. S. Krinchik, V. N. Seleznyov, and M. B. Strugatsky, J. Magn. Magn. Mater. **86**, 105 (1990).

48. M. H. Seavey, Solid State Commun. **10**, 219 (1972).
49. M. B. Strugatsky and K. M. Skibinsky, J. Magn. Magn. Mater. **309**, 64 (2007).
50. V. Preobrazhensky, O. Evstafyev, P. Pernod, and V. Berzhansky, J. Magn. Magn. Mater. **322**, 585 (2010).
51. O. Yevstafyev, V. Preobrazhensky, P. Pernod, and V. Berzhansky, J. Magn. Magn. Mater. **323**, 1568 (2011).
52. V. L. Preobrazhenskii, V. V. Rudenko, F. Perno, and V. I. Ozhogin, JETP Lett. **86**, 348 (2007).
53. J. Zaanen, G. A. Sawatzky, and J. W. Allen, Phys. Rev. Lett. **55**, 418 (1985).
54. W. Schuelke, *Characteristic Valence Electron Excitations. Electron Dynamics by Inelastic X-Ray Scattering* (Oxford Univ. Press, New York, 2007), p. 71.
55. F. de Groot and A. Kotani, *Core Level Spectroscopy of Solids* (CRC, Boca Raton, FL, 2008), p. 512.
56. L. J. P. Ament, M. van Veenendaal, T. P. Devereaux, et al., Rev. Mod. Phys. **83**, 705 (2011).
57. S. G. Ovchinnikov, Phys. Usp. **40**, 993 (1997).
58. I. W. Shepherd, Phys. Rev. B **5**, 4524 (1972).
59. Y. Tanabe and S. Sugano, J. Phys. Soc. Jpn. **9**, 766 (1954).
60. D. T. Sviridov and Yu. F. Smirnov, *Theory of Optical Spectra of Transition Metal Ions* (Nauka, Moscow, 1977) [in Russian].
61. A. G. Gavriliuk, I. A. Trojan, R. Boehler, M. Eremets, A. Zerr, I. S. Lyubutin, and V. A. Sarkisyan, JETP Lett. **75**, 23 (2002).
62. V. A. Sarkisyan, I. A. Troyan, I. S. Lyubutin, A. G. Gavrilyuk, and A. F. Kashuba, JETP Lett. **76**, 664 (2002).
63. A. G. Gavriliuk, I. A. Trojan, S. G. Ovchinnikov, I. S. Lyubutin, and V. A. Sarkisyan, J. Exp. Theor. Phys. **99**, 566 (2004).
64. A. G. Gavriliuk, I. A. Trojan, I. S. Lyubutin, S. G. Ovchinnikov, and V. A. Sarkissian, J. Exp. Theor. Phys. **100**, 688 (2005).
65. I. A. Troyan, M. I. Eremets, A. G. Gavrilyuk, I. S. Lyubutin, and V. A. Sarkisyan, JETP Lett. **78**, 13 (2003).
66. I. A. Troyan, A. G. Gavrilyuk, S. G. Ovchinnikov, I. S. Lyubutin, and N. V. Kazak, JETP Lett. **94**, 748 (2011).
67. S. G. Ovchinnikov, Sov. Phys. Solid State **21**, 1724 (1979).
68. V. V. Val'kov and D. M. Dzebisashvili, JETP Lett. **67**, 289 (1998).
69. V. A. Gavrichkov, S. I. Polukeev, and S. G. Ovchinnikov, Phys. Rev. B **95**, 144424 (2017).
70. V. A. Gavrichkov, S. I. Polukeev, and S. G. Ovchinnikov, J. Exp. Theor. Phys. **127**, 713 (2018).
71. A. M. Kalashnikova, A. V. Kimel, R. V. Pisarev, et al., Phys. Rev. B **78**, 104301 (2008).
72. R. V. Mikhaylovsky, E. Hendry, A. Secchi, et al., Nat. Commun. **6**, 8190 (2015).
73. E. A. Mashkovich, K. A. Grishunin, R. V. Michaylovsky, et al., Phys. Rev. Lett. **123**, 157202 (2019).
74. S. G. Ovchinnikov, V. A. Gavrichkov, S. I. Polukeev, and A. V. Malakhovskii, Phys. Met. Metallogr. **120** (13), 91 (2019).

Translated by K. Shakhlevich